Hindawi
Adsorption Science & Technology
Volume 2022, Article ID 5664344, 13 pages
https://doi.org/10.1155/2022/5664344

Research Article

Synthesis of ZrO_2:Dy^{3+} Nanoparticles: Photoluminescent, Photocatalytic, and Electrochemical Sensor Studies

K. Gurushantha,[1] **K. S. Anantharaju**,[2] **Nagaraju Kottam**,[1] **K. Keshavamurthy**,[3] **C. R. Ravikumar**,[4] **B. S. Surendra**,[2] **A. Murugan**,[5] **and H. C. Ananda Murthy**[6,7]

[1]*Department of Chemistry, M.S. Ramaiah Institute of Technology, Bengaluru 560054, India*
[2]*Department of Chemistry, Dayananda Sagar College of Engineering, Bengaluru 560111, India*
[3]*Department of Physics, Vivekananda Institute of Technology, Bangalore 560074, India*
[4]*Research Center, Department of Science, East West Institute of Technology, Bangalore 560091, India*
[5]*Department of Chemistry, North Eastern Regional Institute of Science & Technology, Nirjuli, Itanagar, 791109 Arunachal Pradesh, India*
[6]*Department of Applied Chemistry, School of Applied Natural Sciences, Adama Science and Technology University, P.O. Box 1888, Adama, Ethiopia*
[7]*Department of Prosthodontics, Saveetha Dental College & Hospital, Saveetha Institute of Medical and Technical Science (SIMAT), Saveetha University, Chennai, 600077 Tamil Nadu, India*

Correspondence should be addressed to C. R. Ravikumar; ravicr128@gmail.com
and H. C. Ananda Murthy; anandkps350@gmail.com

Received 8 April 2022; Revised 21 July 2022; Accepted 2 August 2022; Published 16 August 2022

Academic Editor: Hesham Hamad

Solution combustion was employed to create a series of ZrO_2:Dy^{3+} (1-11 mol percent) nanoparticles (NPs) using oxalyl dihydrazide (ODH) as the fuel. ZrO_2:Dy^{3+} NPs were subjected to calcination at about 700°C. ZrO_2:Dy^{3+} NPs comprised of 1 to 11 mol% of Dy^{3+} were characterized by employing the X-ray diffraction (XRD), transmission electron microscopic (TEM), UV-visible, and X-ray photoelectron spectroscopic (XPS) techniques. The crystallite diameters of 1 to 11 mol% ZrO_2:Dy^{3+} NPs were observed to range from 8.1 nm to 16.3 nm, exhibiting spherical shape. According to BET tests, the pore volume of ZrO_2:Dy^{3+} NPs was determined to be 100.129 cm^3/g. The mean pore diameter of ZrO_2:Dy^{3+} NPs was determined to be 4.803 nm from the Barrett-Joyner-Halenda (BJH) plot. The photoluminescence and photocatalytic dye degradation properties of ZrO_2:Dy^{3+} NPs were investigated. The acid red 88 (AR88) dye was applied to appraise the photocatalytic activities of the NPs under UV irradiation. ZrO_2:Dy^{3+} NPs with 3 mol% Dy^{3+} exhibited improvised photocatalytic activity due to the operative departure of charge carriers. The electrochemical examination of ZrO_2:Dy^{3+} NP modified carbon paste electrode in 0.1 N HCl demonstrated considerable redox potential output, as evidenced by cyclic voltammetric and amperometric measurements. The electrochemical sensor studies on ZrO_2:Dy^{3+} NPs exhibited potentiality towards sensing of highly toxic metals like mercury and lead.

1. Introduction

Because of its outstanding optical and electrical properties, such as strong thermal stability, huge dielectric constant, broad band gap (5–7 eV), and high melting point, zirconium oxide (ZrO_2) was subjected to investigation extensively over the last two decades [1, 2]. Due to its outstanding optical properties, including a high band gap value, a large refractive index, a low optical cost, and improved transparency in the near-infrared and visible ranges, it is a common material in many optical applications [3, 4]. It exhibits a broad band gap and emits photoluminescent (PL) light at short

wavelengths [5]. Materials made of rare-earth-doped oxides have unique optical properties like luminescence efficiency and photochemical stability [6, 7].

Tetragonal, monoclinic, and cubic crystal forms are all found in zirconia. The temperature at which each structure is formed is determined by the synthesis method used and the presence of a dopant of any kind; zirconia produced using the sol–gel process, for example, has an amorphous structure, but it can be transformed into tetragonal zirconia after heat treatment at 500°C. The monoclinic structure begins to appear at 800°C, and at 1300°C, the cubic structure emerges. Zirconia can be utilized in biocomposites, combustible cells, catalytic supports, oxygen detectors, and oxygen sensors [8]. Many researchers have looked into the optical characteristics of Dy-doped ZrO_2. For low concentrations of Dy dopant, zirconia has been reported to have improved photoluminescence (3 mol percent). Gu et al. [9] investigated the consequence of calcinations and doping of Dy^{3+} on ZrO_2 nanoparticle luminescence. They discovered that a concentration of 2% Dy in ZrO_2 produces the extreme comparative luminescence intensity having wavelength of 480 nm. The effective photoluminescence in nanocrystalline zirconia was reported at low Dy concentrations [10].

For the production of ZrO_2:Dy^{3+} in this study, the combustion solution method was used (1-11 mol). The crystalline nature and morphological characteristics of the material were studied using a variety of characterization techniques.

The significant and amazing method of removing contaminants from water and wastewater has been photocatalysis. Under UV light illumination, the produced nanomaterial's catalytic activity for the destruction of acid red 88 (AR88) was evaluated. The photocatalytic activities were explained in relation to the photoluminescence studies and crystallite size, and their applicability in display applications was examined in depth. In 0.1 N HCl solution, cyclic voltammetric and amperometric investigations were also carried out employing electrodes modified with ZrO_2 and ZrO_2:Dy^{3+} (3 mol). Under the detection limit of 2.3602×10^{-3} mol/L, the material demonstrated outstanding catalytic activity for mercury and lead sensing.

2. Experimental

Zr and Dy were obtained from the basic precursors, zirconium (IV) oxynitrate hydrate ($ZrO(NO_3)_2{\cdot}H_2O$: 99.9 percent, S D Fine) and dysprosium (III) oxide (Dy_2O_3: 99.9 percent, Merck). The fuel was made in our lab and is called oxalyl dihydrazide (ODH: $C_2H_6N_4O_2$). For synthesis, oxalic acid, glycine, urea, citric acid, and other fuels were used. ODH with a low ignition temperature produces low molecular weight, innocuous gases as compared to other fuels. Oxide materials produced using ODH as a fuel can be used for a variety of purposes [11, 12]. Initially, Dy_2O_3 is converted to dysprosium nitrate by the dissolution of required quantity of Dy_2O_3 in HNO_3 (1 : 1) for the synthesis of ZrO_2:Dy^{3+} (1–11 mol percent). After the reaction on a sand bath at 80°C was finished, the excess nitric acid was evaporated to produce a transparent terbium nitrate solution.

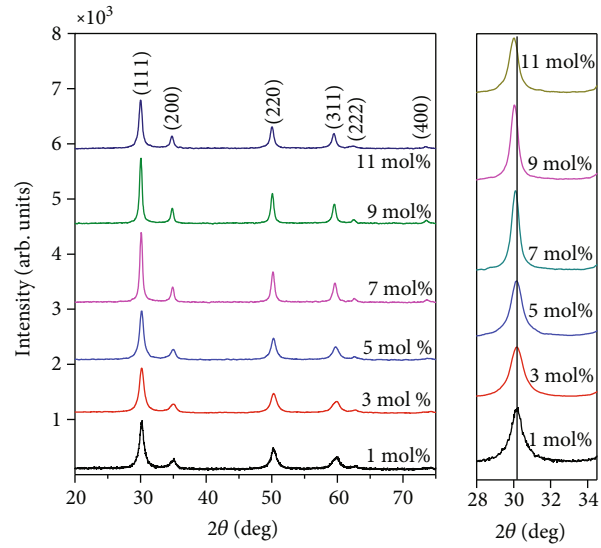

Figure 1: X-ray diffraction pattern of Dy^{3+}-doped (1-11 mol%) ZrO_2 NPs.

The required amounts of ODH and zirconium (IV) oxynitrate hydrate solution were added to the dysprosium nitrate solution while being continuously stirred to achieve smooth mixing. This heterogeneous mixture (redox) was placed on a Petri plate and introduced into a muffle furnace set to 400°C. The decomposition of the mixture eventually unfolds, culminating in the release of large volumes of gases such as CO_2, H_2O, and N_2. The entire procedure consumes about 5 minutes and leads to the production of ZrO_2:Dy^{3+} nanophosphor.

3. Results and Discussion

3.1. Powder X-Ray Diffraction Analysis. XRD experiments were conducted in order to understand the crystalline nature and true crystallite size of Dy-doped ZrO_2 NPs. PXRD patterns of as-synthesised ZrO_2:Dy^{3+} NPs have been found to be very similar to the pattern as per standard JCPDS card no. 81-1551. The cubic phase of ZrO_2 was used to index all of the diffraction patterns (Figure 1). Cubic, monoclinic, and tetragonal polymorphs of ZrO_2 exist in three different crystalline forms. The cubic/tetragonal phase [13] is the most suitable for technological uses among these. Only the peak associated to ZrO_2 was found after doping ZrO_2 with Dy^{3+}. There were no other peaks corresponding to Dy $(NO_3)_3$ or other contaminants, showing that Zr^{4+} ions in the ZrO_2 matrix were replaced by Dy^{3+} ions. A slight peak shift has been observed for ZrO_2 upon Dy doping, which is possibly due to lattice modification and corresponding strain.

Using full width at half maximum (FWHM) data, $D = k/\cos\theta$ [10], the average crystallite size (D) was deduced by applying Scherrer's formula, where k is a constant (approximately 0.90), the X-ray wavelength is 0.15418 nm, and θ is the diffraction angle. The diameters of ZrO_2 crystallite Dy^{3+} (1-11 mol percent) NPs were observed to be between 8.3 and 13.8 nm in size (Table 1).

Table 1: Crystallite sizes of ZrO_2:Dy^{3+} (1-11mol%) NPs.

Samples	Crystallite size (nm)		Strain (ε) $\times 10^{-3}$	SF	δ (10^{16} lin m^{-2})
	Scherrer's formula	W–H plot			
ZrO_2:Dy^{3+} (1mol%)	8.3	9.3	14.3	0.3973	1.451
ZrO_2:Dy^{3+} (3mol%)	9.3	6.4	15.1	0.3971	1.156
ZrO_2:Dy^{3+} (5mol%)	10.2	6.9	9.61	0.3974	0.961
ZrO_2:Dy^{3+} (7mol%)	14.9	9.1	4.47	0.3979	0.450
ZrO_2:Dy^{3+} (9mol%)	16.3	5.3	3.73	0.3982	0.376
ZrO_2:Dy^{3+} (11mol%)	13.8	6.6	5.20	0.3984	0.525

Additionally, Dy doping induces a gradual loss of crystallinity of ZrO_2, due to lattice instability and induced strain on the lattice. Previously, the FWHM was assumed to represent a linear combination of crystallite size and lattice strain components [14]. Equation (1) can be used to express the influence of crystallite size and strain on the FWHM.

$$\beta \cos\theta = \varepsilon (4 \sin\theta) + \frac{\lambda}{D}, \quad (1)$$

where β, θ, λ, and ε are FWHM in radians, Bragg angle, wavelength, and strain associated with the NPs, respectively.

A straight line between 4 sin (x-axis) and cos (y-axis) is shown in equation (1) (Figure 2).

The line's intercept (0.90/D) on the y-axis is determined by the crystallite size, and the strain (ε) determines the line's slope (D). The tiny variations in the numbers were attributable to Scherrer's calculation assuming that the strain component was minimal, and the observed broadening of the diffraction peak was credited only to grain size reduction. With a rise in Dy^{3+} concentration, the strain alters. Table 1 lists the results for other structural features such as dislocation density (δ) and stacking fault (SF) using the following equations [15]:

$$\delta = \frac{1}{D^2}, \quad (2)$$

$$\mathrm{SF} = \left[\frac{2\pi^2}{45(3\tan\theta)^{1/2}}\right], \quad (3)$$

$$\sigma_{\text{stress}} = \frac{\text{microstrain}}{2} \times E, \quad (4)$$

where E is the elastic constant (Young's modulus) of the nanomaterial = 186.21 GPa [16].

The presence of the estimated microstrain in the majority of the planes in the current study suggested the presence of tensile stress on the particle's surface. The residual stress was tensile, with a positive microstrain, causing the PXRD patterns to move to the lower angle side.

3.2. Morphological Studies. Figure 3 depicts the SEM images of ZrO_2:Dy^{3+} (1-11 mol percent) NPs. Because of the large number of gasses generated during combustion, the surface morphology of ZrO_2:Dy^{3+} NPs reveals the presence particle agglomeration which rises with increasing Dy concentration.

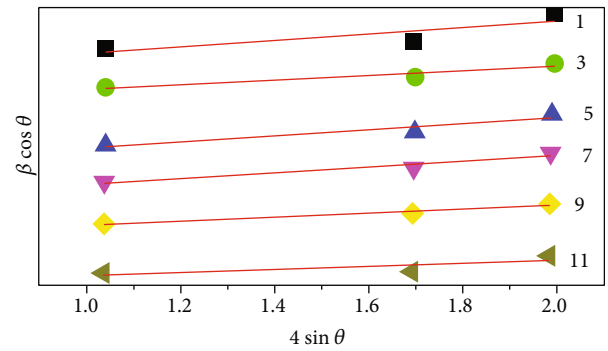

Figure 2: W–H plots of as-formed ZrO_2:Dy^{3+} (1–11 mol%) NPs.

Figure 4(a) depicts the TEM micrograph of ZrO_2:Dy^{3+} (3 mol percent) NM with considerable aggregation of nearly spherical nanocrystals. The recorded crystallite size matched the PXRD data perfectly. A HRTEM image captured from a specific location in Figure 4(b) showed the (111) plane crystal facet of cubic zirconia. The interplanar spacing values of 0.294 nm displayed the (111) plane of cubic zirconia. SAED pattern of ZrO_2:Dy^{3+} (Figure 4(c)) (3 mol%) NM represents cubic ZrO_2 diffraction rings generated from planes (111), (200), (220), and (311) due to cubic zirconia polycrystalline diffraction (Figure 4(b)). The single and pure crystalline cubic ZrO_2 serves as evidence of the value of the current synthesis procedure in producing cubic ZrO_2 NM with good compact size, high purity, and high crystallinity.

Figure 5 shows the nitrogen adsorption-desorption isotherms of BET and BJH plots (inset), respectively. The IUPAC classifications' type IV adsorption isotherms are conformed to by the BET plot for the substance [14]. Type IV adsorption isotherms are frequently produced by mesoporous materials, showing the presence of layer-by-layer adsorption on smooth surfaces [15, 16]. The materials' specific surface area, commonly performed within the linear plots, approximately ranging from $0.05 < P/P0 < 0.3$ [17] is 100.129 m^2/g. Besides, the materials also have H2 type hysteresis loop in accordance with the IUPAC classification [17]; the H2 type hysteresis loop indicates the presence of narrow pore cavity distribution with wide neck size [15]. The BJH plots also confirm the mesoporous nature of the materials with the pore volume and pore diameter values of 0.151 cc/g and 4.803 nm, respectively.

The XPS technique was used to evaluate the elemental composition, chemical states, and elemental bonding for

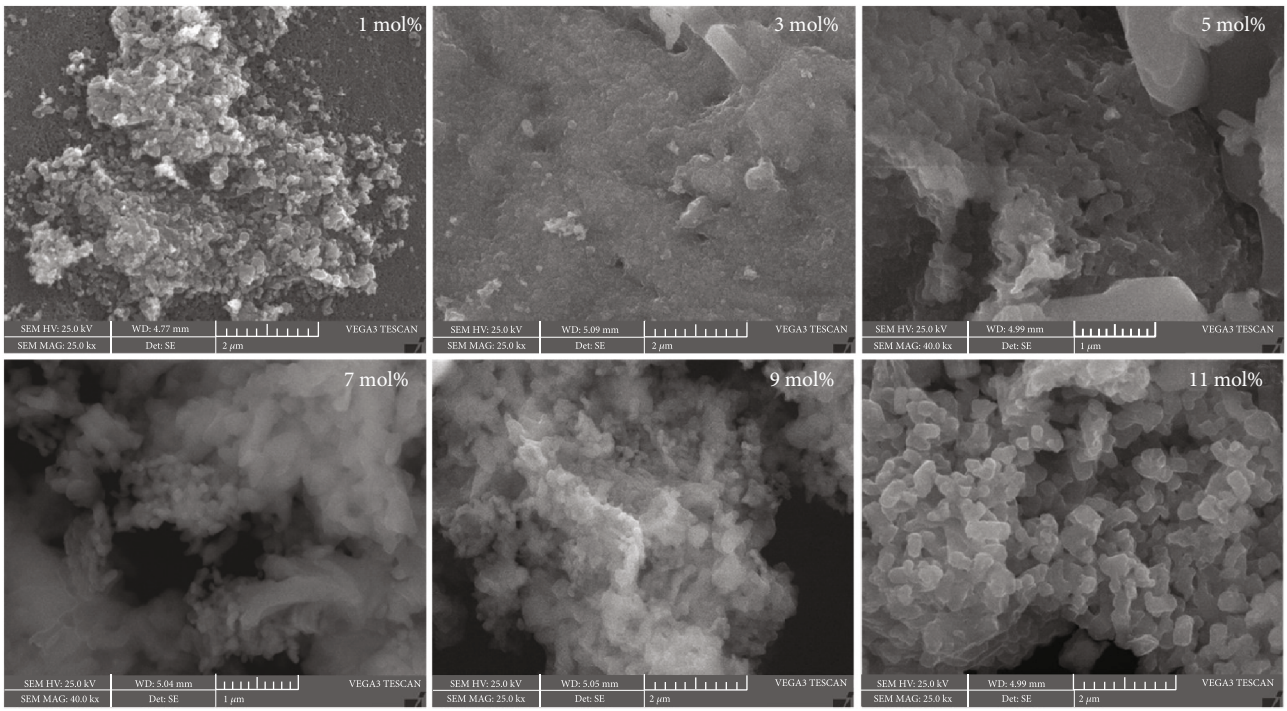

Figure 3: SEM images of ZrO_2:Dy^{3+} (1–11 mol%) NPs.

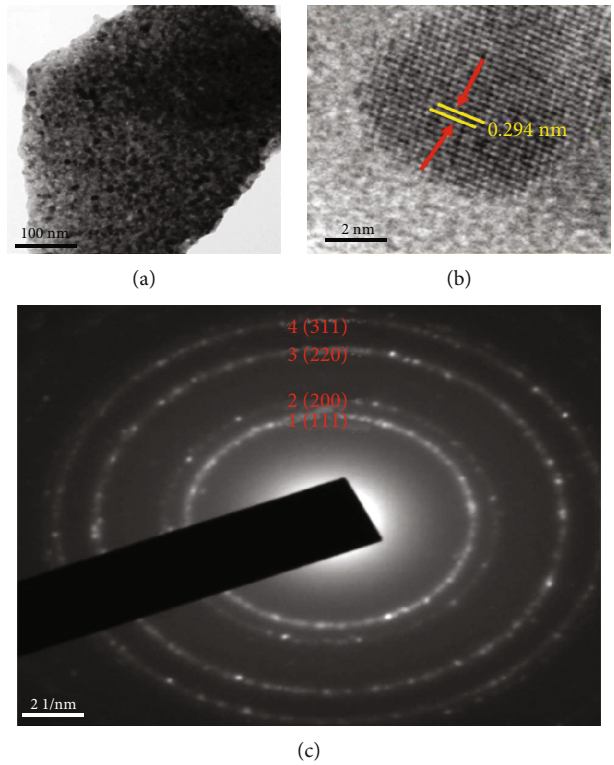

(a) (b)

(c)

Figure 4: (a) TEM image, (b) HRTEM image, and (c) SAED pattern of ZrO_2:Dy^{3+} (3 mol%) NPs.

the produced ZrO_2:Dy^{3+} (3 mol percent), as shown in Figure 6. The recorded wide spectrum of the NM displayed the existence of binding energies ~1072, ~537.6, ~292.2, and~186.3 eV which corroborates to Dy 3d, O 1s, C 1s, and Zr 3d peaks, respectively.

3.3. Photoluminescence (PL) Studies. Exploration of the energy levels inside the band gap positions yielded crucial knowledge from PL research. PL emission can be used to analyse the effectiveness of migration, charge carrier entrapment, and the destiny of photogenerated electron-hole pairs

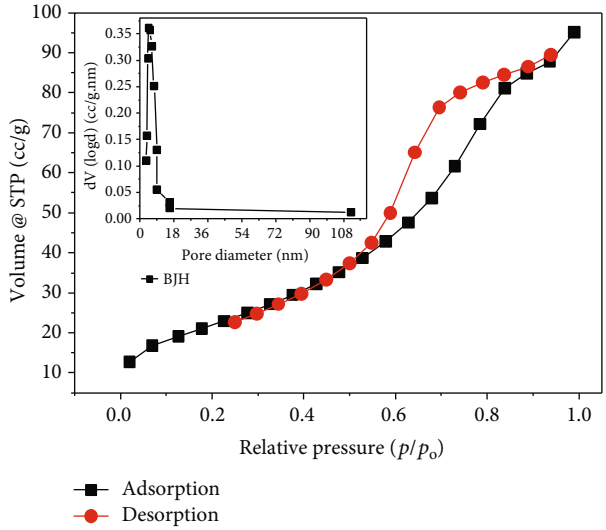

Figure 5: Adsorption-desorption measurements showing BJH plot (inset: pore size distribution).

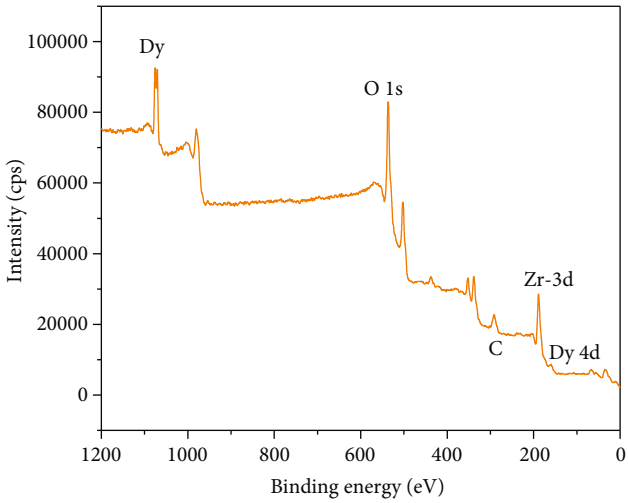

Figure 6: XPS spectra of Dy-doped (3 mol%) ZrO+ NPs.

in semiconductors [18–20]. Because PL emission caused excited electron-hole pairs to recombine, effective separation of charge carrier resulted in a decrease in PL intensity [21, 22].

A PL excitation (PLE) spectrum of 3 mol% Dy^{3+}-doped ZrO_2 nanophosphor measured at a fixed emission wavelength of 580 nm corresponds to the electronic transition ($^4F_{9/22} \rightarrow {}^6H_{13/2}$). The PLE bands at 320, 353, 367, 386, 393, and 416 nm were considered to the electronic transitions of $^6H_{15/2} \rightarrow {}^4H_{11/2}$, $^4M_{17/2}$, $^4G_{11/2}$, $^4I_{5/2}$, $^4F_{9/2}$, and $^4I_{13/2}$, respectively. The energy transfer between central oxygen and the f-f transitions of the Dy^{3+} ions are what causes the former band and are attributed to the host's absorption bands. It proves that the phosphor may be effectively activated by near-UV wavelengths, enabling its use in the creation of white LEDs. Figure 7 displays the emission spectra of ZrO_2:Dy^{3+} phosphors stimulated at 353 nm with 1 to 11 mol percent of Dy^{3+}.

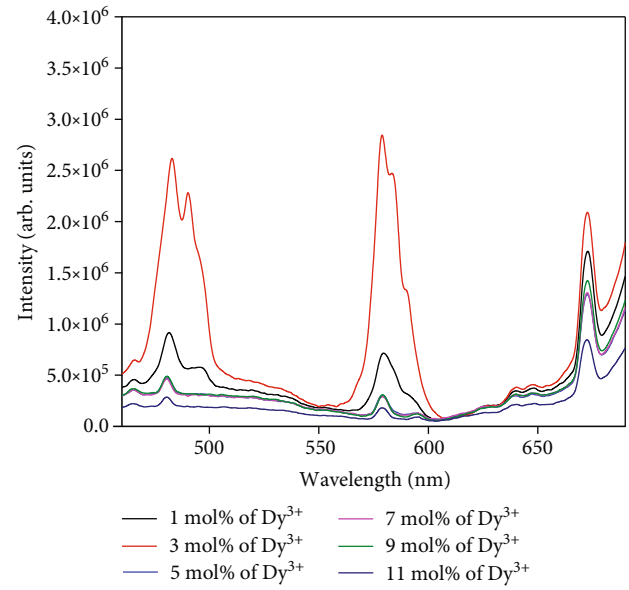

Figure 7: PL emission spectrum of ZrO_2:Dy^{3+} (1–11 mol%) NMs excited at 353 nm.

Table 2: Kinetic studies under UV light for ZrO2:Dy^{3+} (1–11mol%) photocatalysts.

Photocatalysts	Under UV light $k \times 10^{-3}$min^{-1}	%D
ZrO_2:Dy^{3+1}mol%	10.95	73.42
ZrO2:Dy^{3+3}mol%	21.57	82.65
ZrO2:Dy^{3+5}mol%	22.76	75.55
ZrO2:Dy^{3+7}mol%	23.9	79.45
ZrO2:Dy^{3+9}mol%	31.67	80.52
ZrO2:Dy^{3+1}1mol%	20.09	84.00

When activated with 352 nm, all of the peaks were observed to be Dy^{3+}'s emission peaks, exhibiting energy efficient transfers from the host to Dy^{3+}. The luminescence centers stimulated by Dy^{3+} ions were thought to be responsible for the PL spectrum [23]. With the exception of the PL emission intensity, there were essentially insignificant changes in the emission spectra as the Dy^{3+} doping concentration was raised. The peaks observed at 483 nm (blue), 580 nm (yellow), and 672 nm (red) consist of Dy^{3+} transitions corresponding to $^4F_{9/2} \rightarrow {}^6H_{15/2}$, $^4F_{9/2} \rightarrow {}^6H_{13/2}$, and $^4F_{9/2} \rightarrow {}^6H_{11/2}$, respectively. The blue emission corresponding to $^4F_{9/2} \longrightarrow {}^6H_{15/2}$ is due to the magnetic dipole (MD) transition which adheres to the selection rule $\Delta J = 0, \pm 1$ and $0 \leftrightarrow 0$ is a forbidden transition. Meanwhile, the yellow ($^4F_{9/2} \longrightarrow {}^6H_{13/2}$) emission corresponds to the forced electric dipole (ED) transition, which follows the selection rule of $\Delta L = \pm 2$ and $\Delta J = \pm 2$. This transition is significantly impacted by the surrounding environment, and its intensity is decided by the host and also observed that the feeble red emission for ($^4F_{9/2} \longrightarrow {}^6H_{11/2}$) transition belongs to the electric dipole transition. Dy^{3+} ion transitions from the $^4F_{9/2}$ energy level to the overlying energy levels $^6H_{15/2}$, $^6H_{13/2}$,

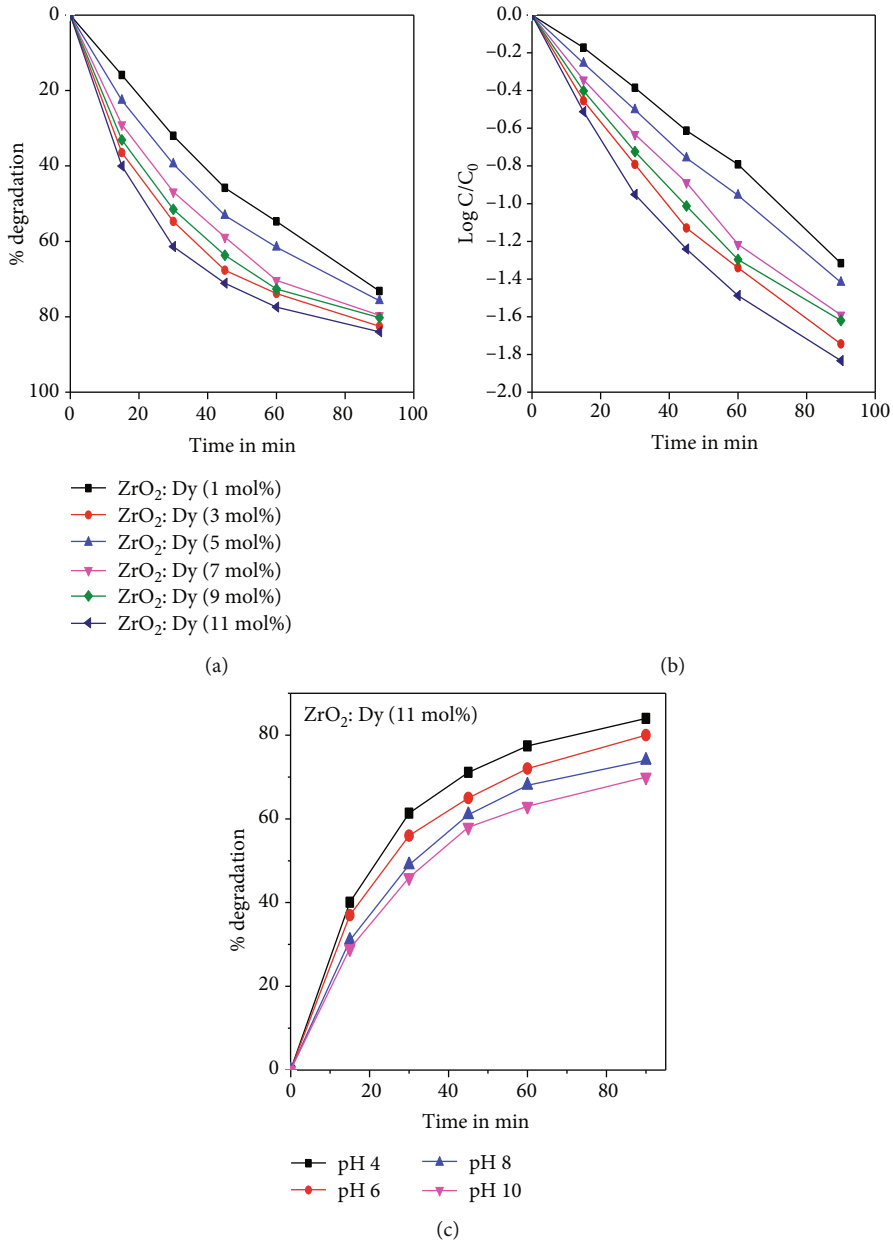

Figure 8: (a) Percentage degradation and (b) C/CO for the decolorization of acid red 88 dye under UV light illumination. (c) Effect of pH on photocatalytic degradation of ZrO_2:Dy (11 mol%) catalyst.

and $^6H_{11/2}$ emit PL. The Dy^{3+} ion's crystal field strength has little effect on the MD transition, while the ED transition can only occur when the Dy^{3+} ion has low symmetry and no inversion center. The intensity of emission increases up to 3 mol percent with an increase in Dy^{3+} concentration from 1 to 11 mol percent before decreasing as a result of concentration quenching. This will clearly show how the PL emission is impacted by the concentration of dopant ions. In fact, luminescence quenching is caused by energy migration, ionic interactions, and cross relaxation to ground energy states, all of which are due to higher concentration of dopant, resulting in the reduction in the mean distance between dopant ions and, in some cases, the creation of dopant clusters. Nevertheless, the excellent emission property of ZrO_2:Dy^{3+} sample shows that it can be used for display application [24].

3.4. Photocatalytic Activity of Acid Red 88 (AR88) Dye under UVA/Sunlight. To investigate the photodegradation activity of Dy^{3+}-doped ZrO_2 (1-11 mol percent) NPs, the decolorization of hazardous azo acid red 88 dye was conducted under UV light irradiation for 90 minutes. Acid red 88 degradation was found to be minimal in the absence of ZrO_2:Dy^{3+} and under dark condition. As a consequence, the photocatalytic activity of the excited semiconductors is primarily responsible for the decolorization of the dye.

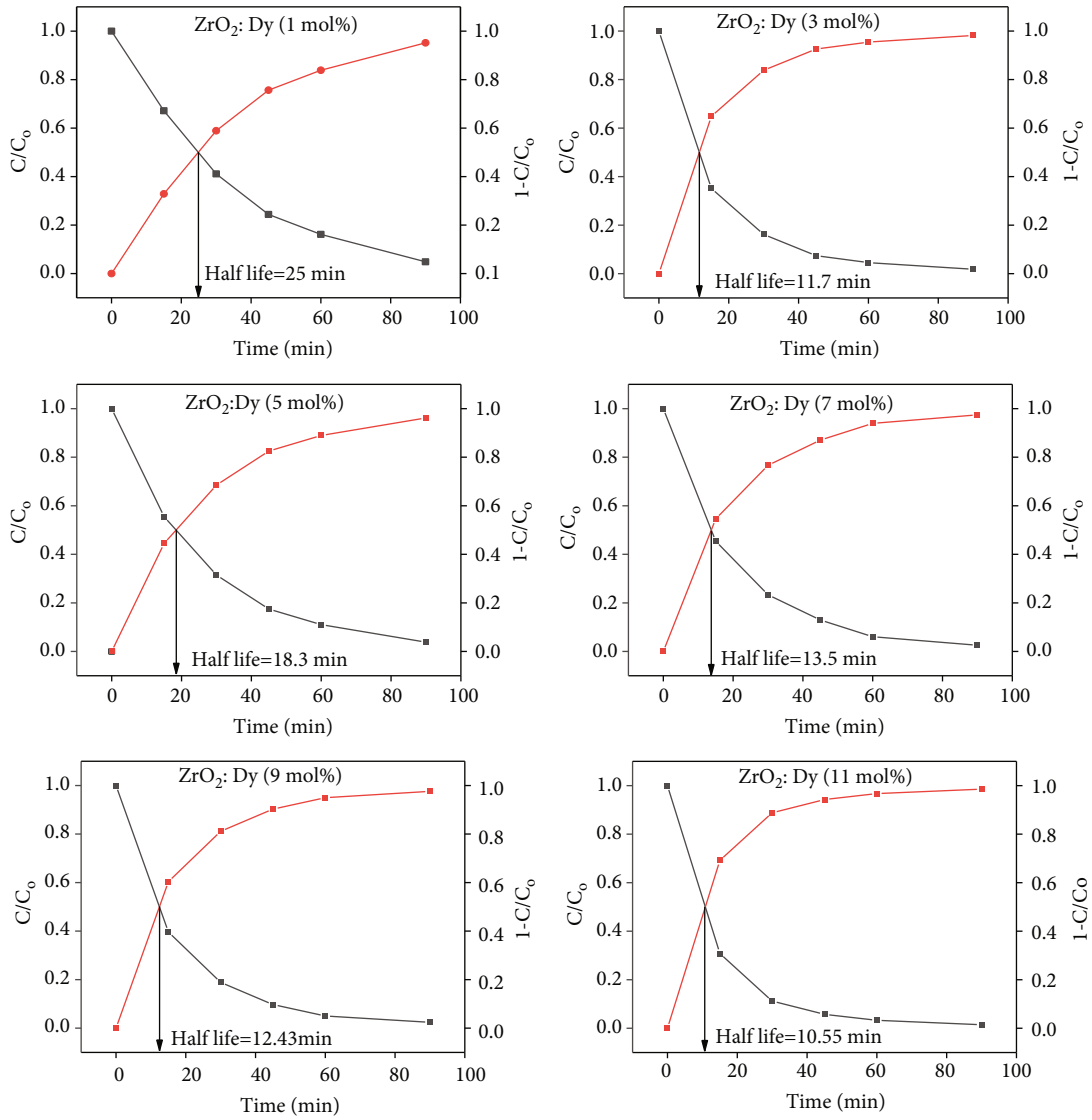

Figure 9: Half-life plot for the AR88 dye under UV irradiation in the presence of ZrO_2:Dy^{3+} (1-11 mol%) photocatalyst.

Table 3: Summary of the photocatalytic degradation of various photocatalysts and dyes.

Photocatalysts	Light	Dye	Degradation	Ref.
$TaON/Bi_2MoO_6$	Visible light	Levofloxacin	92.7% (75min)	[29]
SiO_2-Bi_2MoO_6	Visible light	Methyl blue	86.3% (4.5 hours)	[30]
WNR/TNB	Solar light	Rhodamine B (RhB)	96% (80min)	[31]
SCNT6	Xenon lamp irradiation	Congo red	96.2% (60min)	[32]
Ag_2O/TiO_2 (4 : 10)	UV	Methyl orange	93% (6min)	[33]
ZrO_2-doped TiO_2	UV	Rhodamine B	96.3% (60min)	[34]
ZrO_2-doped TiO_2 at 1%wt	UV	Methyl orange and rhodamine B	78.1 and 75.5%	[35]
ZrO_2:Fe^{3+} (2 mol%)	UV	Acid orange 7	98% (90min)	[18]
ZrO_2:Sm^{3+11}mol%	Solar light	Acid green G	83.8% (90min)	[36]
ZrO2:Dy^{3+11}mol%	UV	Acid red 88	84% (90min)	Present work

Under UV light, the percentage of acid red 88 decolorization catalyzed by ZrO_2:Dy^{3+} photocatalysts is shown in Table 2. Acid red 88 decolorization rises with increasing dopant concentration up to 11 mol% under UV light, implying that 11 mol% Dy-doped NPs were efficient in separating photo-emitted electron-hole pairs to enhance

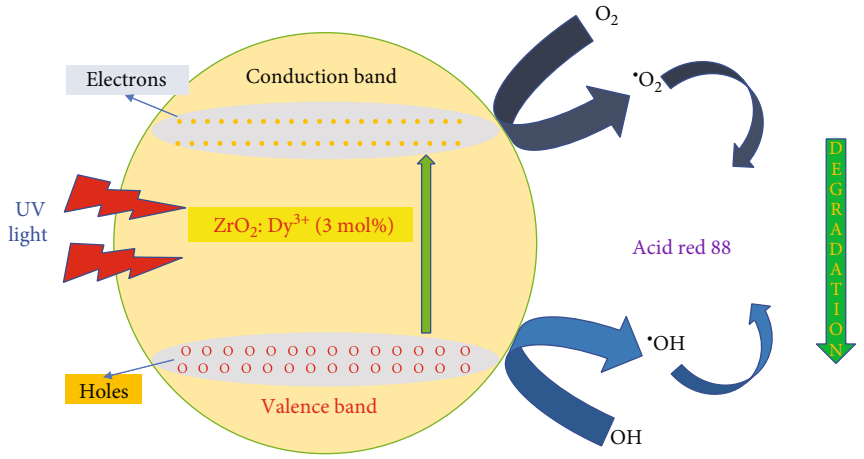

Figure 10: Proposed mechanism for the photocatalytic decolorization of AR88 dye over the ZrO_2:Dy^{3+} photocatalyst.

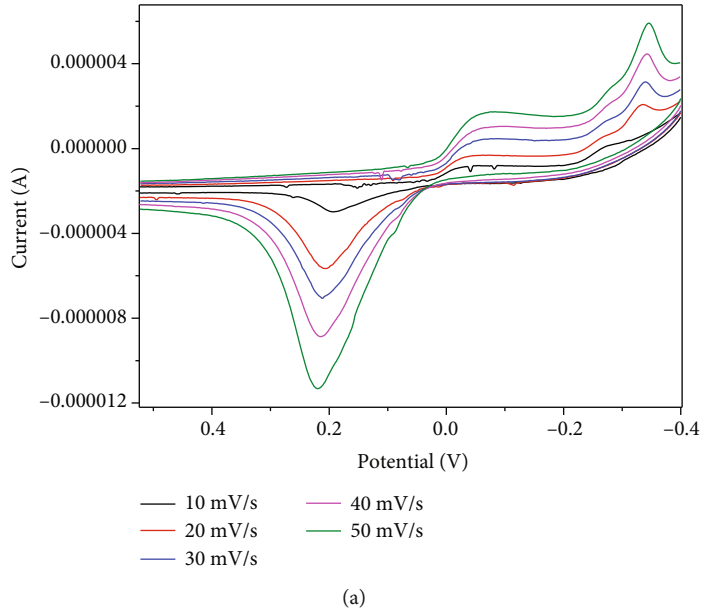

(a)

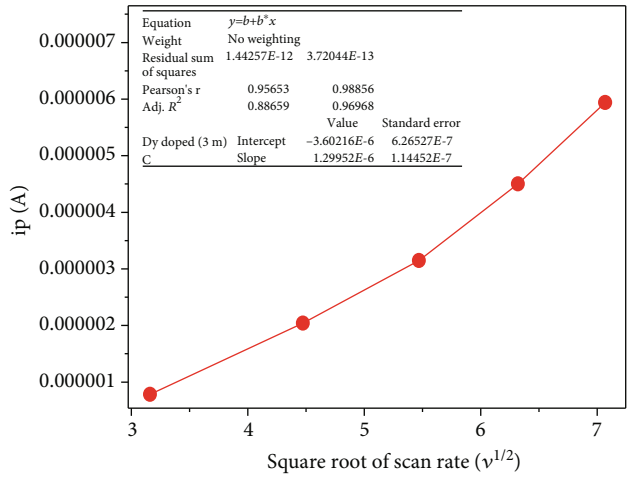

(b)

Figure 11: Cyclic voltammogram of Dy-doped (3 mol%) ZrO_2 sample at different scan rates v/s silver-silver chloride electrode. (b) A plot of cathodic peak current (ip) and the square root of scan rate ($v_{1/2}$) for Dy^{3+}-doped (3 mol%) ZrO_2 electrode.

Table 4: Oxidation potential (E_O), reduction potential (E_R), the difference between E_O and E_R, diffusion coefficient of Dy^{3+}-doped ZrO_2 (1–11 mol%) electrodes.

Name of the sample	E_O (V)	E_R (V)	E_O (V) – E_R (V)
1% Dy^{3+}-doped ZrO_2	0.3732	0.0204	0.3528
3% Dy^{3+}-doped ZrO_2	0.4536	0.3824	0.0712
5% Dy^{3+}-doped ZrO_2	0.4812	0.3741	0.1071
7% Dy^{3+}-doped ZrO_2	0.1808	-0.0792	0.2600
9% Dy^{3+}-doped ZrO_2	0.2048	-0.0436	0.2484
11% Dy^{3+}-doped ZrO_2	0.2039	-0.0511	0.2550

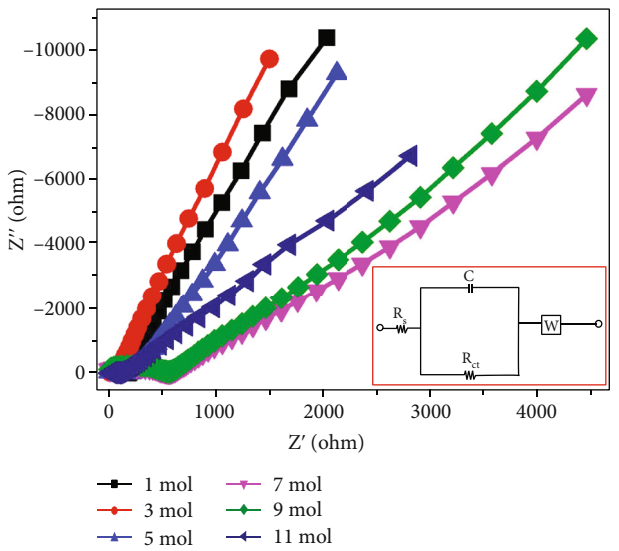

Figure 12: Nyquist plots of Dy^{3+}-doped ZrO_2 (1–11 mol%) electrodes.

the photocatalytic degradation efficiency. Acid red 88 was decolorized under solar light with ZrO_2:Dy^{3+} catalysts in the following order: ZrO_2 : Dy^{3+} (11 mol%) > ZrO2 : Dy^{3+} (3 mol%) > ZrO2 : Dy^{3+} (9 mol%) > ZrO2 : Dy^{3+} (7 mol%) > ZrO2 : Dy^{3+} (5 mol%) > ZrO2 : Dy^{3+} (1 mol%) and is shown in Figures 8(a) and 8(b) and Table 2.

These findings imply that in the ZrO_2 lattice, an optimal dopant concentration of Dy^{3+} exists, resulting in effective charge carrier separation. To check the performance of photocatalyst under the effect of pH, 11 mol% ZrO2:Dy^{3+} NPs were assessed on the removal of acid red 88 at different values of pH. As the pH decreases, degradation of AR88 increases as shown in Figure 8(c). In acidic medium, photocatalytic activity increases due to the anionic nature of AR88 dye. An electrostatic force is generated between protonated surface of the catalyst ZrO_2:Dy in acidic medium and anionic dye AR88. Hence, dye adsorption on the catalyst surface is enhanced and photodegradation increases. In alkaline medium, there is repulsion between the negatively charged ZrO_2:Dy and anionic dye AR88 molecule; hence, percentage of degradation is less in alkaline medium compared to acidic medium.

Table 5: EIS data of Dy^{3+}-doped ZrO_2 (1–11 mol%) electrodes.

Name of the sample	R_S (V)	R_{ct} (V)	C_{dl} (F)
1% Dy^{3+}-doped ZrO_2	1.948	161.34	0.000226
3% Dy^{3+}-doped ZrO_2	0.862	79.32	0.01512
5% Dy^{3+}-doped ZrO_2	1.594	94.43	0.003541
7% Dy^{3+}-doped ZrO_2	2.595	99.64	0.000865
9% Dy^{3+}-doped ZrO_2	2.578	110.52	0.000642
11% Dy^{3+}-doped ZrO_2	4.691	194.46	0.000835

Increasing the amount of Dy^{3+} in the catalyst structure resulted in a greater surface barrier and a narrower space charge area, allowing the generated electron-hole pairs to be separated efficiently. Increases in Dy^{3+} concentration up to a certain point cause the space charge layer to be breached, allowing light to penetrate deeper into ZrO2:Dy^{3+} nanoparticles are a type of Dy^{3+} nanoparticle [25]. The half-life of the degradation was calculated for each dopant, and it was found to be 25 min, 11.7 min, 18.3 min, 13.5 min, 12.43 min, and 10.55 min for 1, 3, 5, 7, 9, and 11 mol%, respectively. The respective results are shown in Figure 9. In comparison to the other dopants as mentioned in Table 3, the half-life required for degradation by 3 mol% and 11 mol% was substantially shorter. Hence, it can be concluded that the best suitable dopant for the degradation was 11 mol%.

According to the proposed mechanism, when light energy strikes the catalyst's surface, the electron in the valence band (VB) is stimulated to the empty conduction band (CB) (Figure 10), resulting in the production of electron-hole, which further react with the pollutant causing the formation of hydroxyl radicals or singlet oxygen radicals or holes which are responsible for the pollutant degradation [26–28].

When the migration occurs, these electron-hole pairs will be involved in the redox reaction. When holes combine with the hydroxide ion, it results in the formation of hydroxyl radicals, whereas the superoxide and hydrogen peroxide were produced due to the interaction of electrons with oxygen in the system. The produced superoxide and hydrogen peroxide react together by producing the hydroxyl radicals. In the final step, the produced radicals will react with the pollutant on the metal surface by forming the intermediate compounds in a short time. Finally, these radicals will help in the breakdown of the pollutant to form CO_2 and H_2O.

The 11mol% ZrO2:Dy^{3+} NP reusability test was carried out with an AR88 concentration of 10 ppm, a photocatalyst dosage of 60 mg, and a reaction period of 90 min. To calculate the degrading efficiency loss after each run, six consecutive runs were made. The percentage of degradation for six cycles is 84%, 84%, 83.1%, 82.9%, 82.8%, and 82%, respectively. Even after the sixth run, the degrading efficiency barely decreased may be due to the loss of catalyst during filtration of the catalyst for the next cycle. It was shown that 11 mol% ZrO2:Dy^{3+} NPs can be an effective photocatalyst with high reusability potential for the degradation of AR88 [37–44].

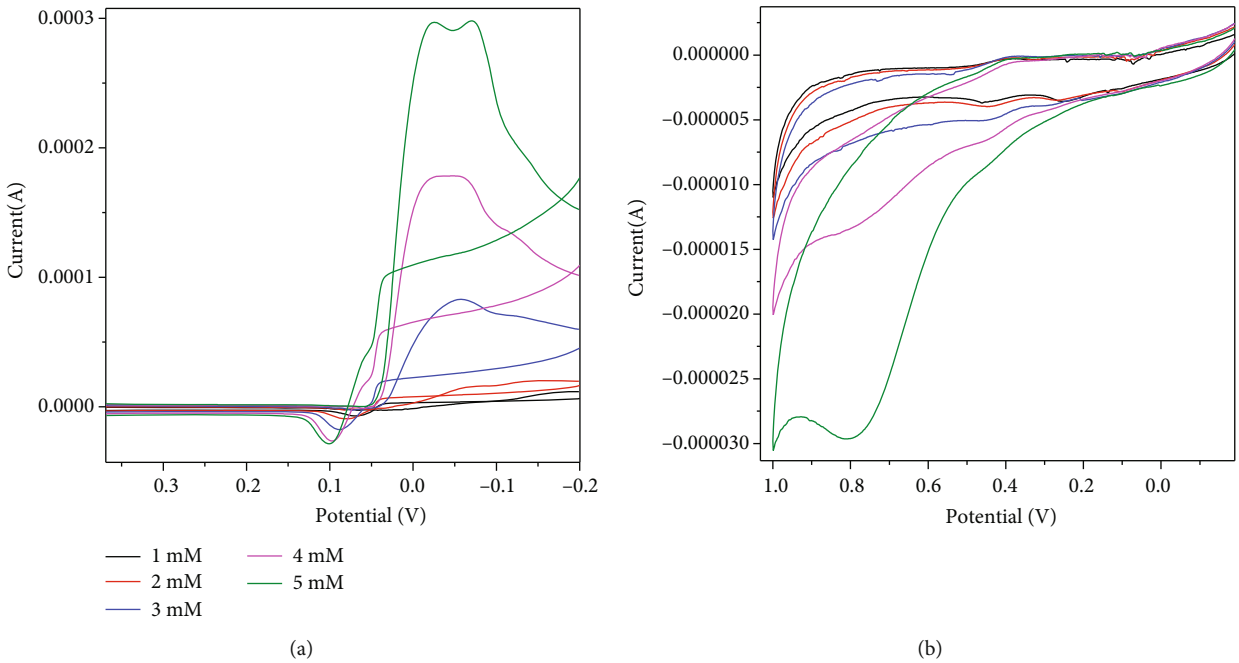

Figure 13: Cyclic voltammogram of ZrO_2:Dy^{3+} (3 mol%) NP detection of (a) mercury and (b) lead of concentration range 1-5 mM.

3.5. Electrochemical Sensor Study

3.5.1. Carbon Paste Electrode. To make a carbon paste electrode, a mixture of the prepared sample Dy^{3+}-doped ZrO_2, graphite powder, and silicon oil (mass ratio of 15 : 70 : 15) was crushed in a mortar for 20 minutes. This powder was then gently pressed into a Teflon hollow tube (0.3 mm surface area) for further research [45].

3.5.2. Electrochemical Studies. Cyclic voltammetric measurements were performed using the three-electrode assembly in a 50 mL beaker chamber at room temperature. The energetic electrode material ZrO_2 undergoes a few strong Faradaic reactions that lead to a few strong redox peaks [46]. The CV activity of a (3 mol percent) sample in 1 N HCl at different moles using -0.4 to 0.6 V potentials and scan rates of 10 to 50 mV (Figure 11(a)) has been investigated. The observed capacitance was far from that of a typical double-layer electrical conductor, which typically displays a rectangular CV curve.

The linear connection between cathodic peak current (ip) and scan rate ($v_{1/2}$) (Figure 11(b)) demonstrates that hydrogen diffusion limits the electrode reaction of Dy^{3+}-doped ZrO_2 electrodes. The constructed electrode's hydrogen diffusion coefficient (D) was calculated using the slope of the fitted line in Figure 11(b). The value of D is 1.299×10^{-6} cm^2s^{-1}.

The greatest potential difference between the anodic (E_O) and cathodic (E_R) peaks for particular moles is a good predictor of redox reversibility. From Table 4, the ZrO_2 sample with 3 mol% Dy^{3+} dopant has the lowest value, 0.0712 V, which is small when compared to other doped samples, indicating that it is more reversible [47].

Figure 12 shows the electrochemical impedance spectra of Dy^{3+}-doped ZrO_2 (1–11 mol percent) electrodes with a frequency range varying from 1 Hz to 1 MHz and a 5 mV amplitude. The spectra show a high-frequency load transfer resistance and a low-frequency slope associated with the Warburg resistance. The resistance of the ZrO_2 electrode with Dy^{3+}-doped (3 mol%) additive is substantially lower than that of other Dy^{3+}-doped ZrO_2 electrodes, suggesting that the 3 mol% additional electrode's electrochemical reaction is stronger than that of other electrodes [48]. A high-frequency zone marked by a semicircle depicts charge transport at the electrode/electrolyte interface, as well as a low-frequency zone denoted by a straight line that represents electrode capacitance. The diameter of the semicircle arc on the real axis can be used to calculate the charge transfer resistance R_{ct} [49]. The sample's R_{ct} value is lower because the semicircle arc has a smaller circumference. As the linear curve moves closer to the y-axis, it indicates that the sample has a high capacitance [50].

Additionally, this circumstance is associated to the ideals of R_{ct} and C yielded by circuit fitting (inset of Figure 12). As illustrated in the Nyquist plots, the resistance gauges the high-frequency semicircle of charge transfer (R_{ct}) and the capacitance (C) of the double layer.

Table 5 includes values that were obtained by fitting simulation data with an equivalency circuit and relate to the catalytic properties of active materials, such as solution resistance (R_s), charge transfer resistance (R_{ct}), and double-layer capacitance (C_{dl}). The charge transfer resistance is low due to the surface catalytic activity of the generated electrodes; when ZrO_2:Dy^{3+} is used, the electrode double-layer capacitance is at its highest (3 mol percent) [34].

The cyclic voltammograms of Dy^{3+}-doped ZrO_2 (3 mol%) utilized for mercury and lead sensing are shown in Figure 13. As a consequence, peak position variation due to oxidation and reduction was justified. The

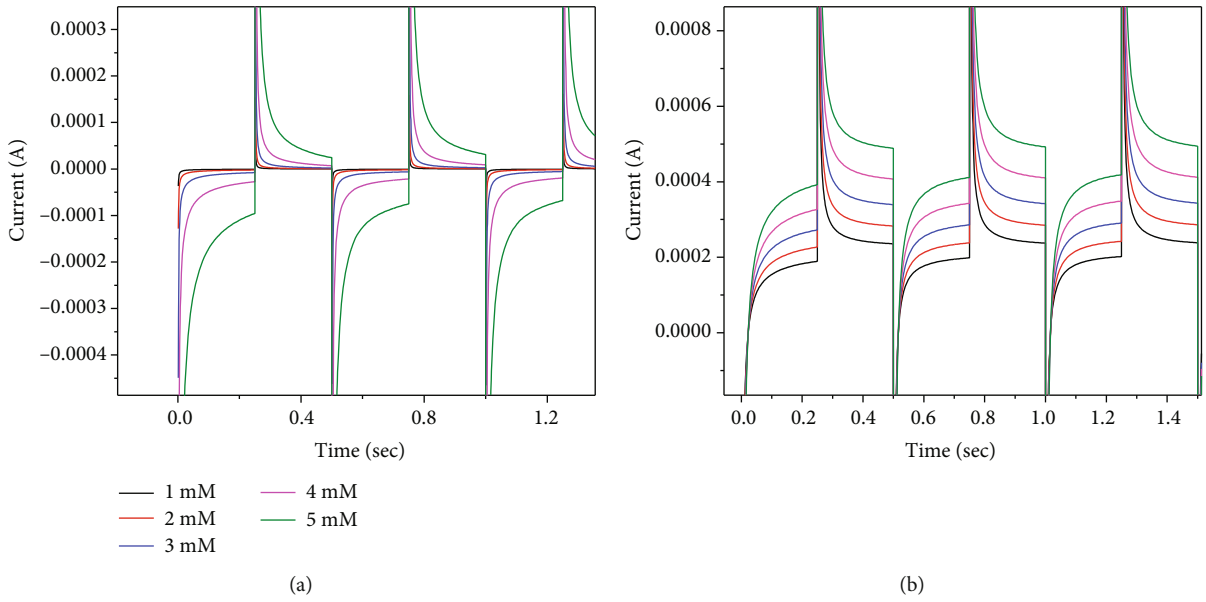

FIGURE 14: Amperometric $i-t$ curve for determination of mercury and lead using ZrO_2:Dy^{3+} (3 mol%).

development of an anodic oxidation peak at 0.1 V and a cathodic reduction peak at -0.05 V during sensing, as well as the disappearance of the oxidation peak at 0.2 V, shows that the manufactured carbon paste electrode is successful in sensing approach for amounts 1-5 mM.

Nevertheless, the cyclic voltammogram of a lead sensor reveals that the entire voltammogram form changes, including the elimination of the oxidation and reduction peaks, but the introduction of an oxidation peak at 0.8 V. For 0 mM mercury and lead, the constructed electrode showed an initial current response of 60 s. Furthermore, the current response increases with continuous introduction of 1 mM mercury and lead (Figure 14), and within the brief time frame of 4 seconds, it approaches a steady current.

This result indicates that the sensor reacts quickly to mercury (0.0003 A) and lead (0.0008 A) oxidation. Finally, the positions of the reduction and oxidation peaks were determined to be considerably different, indicating that the electrodes produced are suitable for sensor applications without impacting other compounds in the sample.

4. Conclusion

A variety of nanoparticles ZrO2:Dy^{3+} (1-11 mol percent) were prepared in this study using a simple and cheap propellant combustion process. The cubic phase of Dy^{3+}-doped ZrO_2 NPs was confirmed by PXRD and HRTEM. The average crystallite size, as determined by Debye Scherrer's and W–H techniques, was found to be between 8.1 and 16.3 nm. The results were very similar to those of the TEM. Under UV light, the photocatalytic activity of ZrO2:Dy^{3+} increased as the concentration of Dy^{3+} rose. All of the photocatalysts displayed increased activity for the breakdown of acid red 88 dye when exposed to UV light. The successful separation of charge carriers was related to the increased activity for the decolorization of acid red 88 under UV radiation. The reversibility of the carbon paste electrode made with Dy^{3+}-doped ZrO_2 NPs was excellent (lower value of $E_O - E_R$). Electrochemical impedance measurements revealed a low charge-transfer resistance, confirming its excellent conductivity. The proton diffusion coefficient (D) value of the Dy^{3+}-doped ZrO_2 electrode material was found to be 1.299×10^{-6} cm^2s^{-1}. These electrodes were particularly successful in sensing heavy metals like mercury and lead in acidic media, according to CV and amperometric studies. The electrode material's quick reaction (3 s) for sensing medicines at concentrations as low as 1 mM was the study's highlight. The study shows that Dy^{3+}-doped ZrO_2 is a viable and economical electrode material for upcoming sensing applications, which might be scaled up for commercialization.

Data Availability

The data used to support the findings of this study are included within the article.

Conflicts of Interest

The authors declare no conflict of interest.

Acknowledgments

We would like to express our deepest regards for the Centre for Advanced Materials & Technology, M.S. Ramaiah Institute of Technology, Bangalore, India, for their support and help toward characterization analysis.

References

[1] L. Liao, J. W. Bai, Y. C. Lin, Y. Q. Qu, Y. Huang, and X. F. Duan, "High-performance top-gated graphene-nanoribbon transistors using zirconium oxide nanowires as high-dielectric-constant gate dielectrics," *Advanced Materials*, vol. 22, pp. 1941–1945, 2010.

[2] M. F. Hanafi and N. Sapawe, "The potential of ZrO_2 catalyst toward degradation of dyes and phenolic compound," *Materials Today: Proceedings*, vol. 19, pp. 1524–1528, 2019.

[3] I. John Berlin, J. S. Lakshmi, S. Sujatha Lekshmy, G. P. Daniel, P. V. Thomas, and K. Joy, "Effect of sol temperature on the structure, morphology, optical and photoluminescence properties of nanocrystalline zirconia thin films," *Journal of Sol-Gel Science and Technology*, vol. 58, no. 3, pp. 669–676, 2011.

[4] I. John Berlin, L. V. Maneeshya, K. Jijimon, P. V. Thomas, and K. Joy, "Enhancement of photoluminescence emission intensity of zirconia thin films via aluminum doping for the application of solid state lighting in light emitting diode," *Journal of Luminescence*, vol. 132, no. 11, pp. 3077–3081, 2012.

[5] I. John Berlin, V. S. Anitha, P. V. Thomas, and K. Joy, "Influence of oxygen atmosphere on the photoluminescence properties of sol–gel derived ZrO_2 thin films," *Journal of Sol-Gel Science and Technology*, vol. 64, no. 2, pp. 289–296, 2012.

[6] T. Ninjbadgar, G. Garnweitner, A. Borger, L. M. Goldenberg, O. V. Sakhno, and J. Stumpe, "Synthesis of luminescent ZrO_2: Eu^{3+} nanoparticles and their holographic submicrometer patterning in polymer composites," *Advanced Functional Materials*, vol. 9, pp. 1819–1825, 2009.

[7] H. Hobbs, S. Briddon, and E. Lester, "The synthesis and fluorescent properties of nanoparticulate ZrO_2 doped with Eu using continuous hydrothermal synthesis," *Green Chemistry*, vol. 11, no. 4, pp. 484–491, 2009.

[8] S. D. Meetei and S. D. Singh, "Hydrothermal synthesis and white light emission of cubic ZrO_2:Eu^{3+} nanocrystals," *Journal of Alloys and Compounds*, vol. 587, pp. 143–147, 2014.

[9] F. Gu, S. F. Wang, M. K. Lu et al., "Effect of Dy^{3+} doping and calcination on the luminescence of ZrO_2 nanoparticles," *Chemical Physics Letters*, vol. 380, no. 1-2, pp. 185–189, 2003.

[10] L. A. D. Torres, E. D. la Rosa, P. Salas, V. H. Romero, and C. A. Chavez, "Efficient photoluminescence of Dy_3+ at low concentrations in nanocrystalline ZrO_2," *Journal of Solid State Chemistry*, vol. 181, no. 1, pp. 75–80, 2008.

[11] S. T. Fardood, F. Moradnia, R. Forootan et al., "Facile green synthesis, characterization and visible light photocatalytic activity of $MgFe_2O_4$@$CoCr_2O_4$ magnetic nanocomposite," *Journal of Photochemistry and Photobiology A: Chemistry*, vol. 423, article 113621, 2022.

[12] M. Muthuraman, N. A. Dhas, and K. C. Patil, "Combustion synthesis of oxide materials for nuclear waste immobilization," *Bulletin of Materials Science*, vol. 17, no. 6, pp. 977–987, 1994.

[13] A. Khataee, R. D. C. Soltani, Y. Hanifehpour, M. Safarpour, H. G. Ranijbar, and S. W. Joo, "Synthesis and characterization of dysprosium-doped ZnO nanoparticles for photocatalysis of a textile dye under visible light irradiation," *Industrial and Engineering Chemistry Research*, vol. 53, no. 5, pp. 1924–1932, 2014.

[14] M. Thommes, K. Kaneko, A. V. Neimark et al., "Physisorption of gases, with special reference to the evaluation of surface area and pore size distribution (IUPAC technical report)," *Chem*, vol. 87, no. 9-10, pp. 1051–1069, 2015.

[15] K. A. Cychosz and M. Thommes, "Progress in the physisorption characterization of nanoporous gas storage materials," *Engineering*, vol. 4, no. 4, pp. 559–566, 2018.

[16] M. Fan, X. Zeng, X. Yang, X. Zhang, and B. Ren, "Rational design of asymmetric supercapacitorsviaa hierarchical core–shell nanocomposite cathode and biochar anode," *RSC Advances*, vol. 9, no. 72, pp. 42543–42553, 2019.

[17] K. S. Walton and R. Q. Snurr, "Applicability of the BET method for determining surface areas of microporous metal –organic frameworks," *American Chemical Society*, vol. 129, no. 27, pp. 8552–8556, 2007.

[18] K. Gurushantha, K. S. Anantharaju, H. Nagabhushana et al., "Facile green fabrication of iron-doped cubic ZrO_2 nanoparticles by _Phyllanthus acidus_ : structural, photocatalytic and photoluminescent properties," *Journal of Molecular Catalysis A: Chemical*, vol. 397, pp. 36–47, 2015.

[19] D. Prakashbabu, R. H. Krishna, B. M. Nagabhushana et al., "Low temperature synthesis of pure cubic ZrO_2 nanopowder: structural and luminescence studies," *Spectrochimica Acta Part A: Molecular and Biomolecular Spectroscopy*, vol. 122, pp. 216–222, 2014.

[20] R. Suresh, V. Ponnuswamy, and R. Mariappan, "Effect of annealing temperature on the microstructural, optical and electrical properties of CeO_2 nanoparticles by chemical precipitation method," *Applied Surface Science*, vol. 273, pp. 457–464, 2013.

[21] L. X. Lovisa, J. Andres, L. Gracia et al., "Photoluminescent properties of ZrO^2: Tm^{3+}, Tb^{3+}, Eu^{3+} powders- a combined experimental and theoretical study," *Journal of Alloys and Compounds*, vol. 695, pp. 3094–3103, 2017.

[22] A. A. Nashivochnikov, A. I. Kostyukov, A. V. Zhuzhgov, M. I. Rakhmanova, S. V. Cherepanova, and V. N. Snytnikov, "Shaping the photoluminescence spectrum of ZrO_2: Eu^{3+} phosphor in dependence on the Eu concentration," *Optical Materials*, vol. 121, article 111620, 2021.

[23] A. King, R. Singh, R. Anand, S. K. Behera, and B. B. Nayak, "Dopant concentration induced tuning of emission in Eu^{3+}-doped zirconia nanoparticles," *Journal of Physics and Chemistry of Solids*, vol. 163, article 110575, 2022.

[24] R. K. Tamrakar, D. P. Bisen, and K. Upadhyay, "Photoluminescence behavior of ZrO_2: Eu^{3+} with variable concentration of Eu^{3+} doped phosphor," *Journal of Radiation Research and Applied Sciences*, vol. 8, no. 1, pp. 11–16, 2015.

[25] A. Martínez-Hernández, J. Guzmán-Mendoza, T. Rivera-Montalvo et al., "Synthesis and cathodoluminescence characterization of ZrO_2:Er^{3+} films," *Journal of Luminescence*, vol. 153, pp. 140–143, 2014.

[26] A. Naveen Kumar, D. M. Jnaneshwara, H. Nagabhushana et al., "Enhanced photoluminescence, electrochemical and photocatalytic activity of combustion synthesized $La_{10}Si_6O_{27}$: Dy^{3+} nanophosphors," *Journal of Science: Advanced Materials and Devices*, vol. 6, pp. 49–57, 2021.

[27] B. N. Lakshminarasappa, S. C. Prashantha, and F. Singh, "Ionoluminescence studies of combustion synthesized Dy^{3+} doped nano crystalline forsterite," *Current Applied Physics*, vol. 11, pp. 1274–1277, 2011.

[28] L. G. Devi, S. G. Kumar, K. M. Reddy, and C. Munikrishnappa, "Effect of various inorganic anions on the degradation of Congo Red, a di azo dye, by the photo-assisted Fenton process using zero-valent metallic iron as a catalyst," *Desalination and Water Treatment*, vol. 4, no. 1-3, pp. 294–305, 2009.

[29] L. Renuka, K. S. Anantharaju, Y. S. Vidya et al., "A simple combustion method for the synthesis of multi-functional ZrO_2/CuO nanocomposites: excellent performance as sunlight photocatalysts and enhanced latent fingerprint detection," *Applied Catalysis. B, Environmental*, vol. 210, pp. 97–115, 2017.

[30] C. Gionco, S. Hernández, M. Castellino et al., "Synthesis and characterization of Ce and Er doped ZrO_2 nanoparticles as

solar light driven photocatalysts," *Journal of Alloys and Compounds*, vol. 775, pp. 896–904, 2019.

[31] C. Pratapkumar, S. C. Prashantha, V. G. Dileep Kumar et al., "Structural, photocatalytic and electrochemical studies on facile combustion synthesized low-cost nano chromium (III) doped polycrystalline magnesium aluminate spinels," *Journal of Science: Advanced Materials and Devices*, vol. 6, no. 3, pp. 462–471, 2021.

[32] S. Li, C. Wang, M. Cai et al., "Facile fabrication of TaON/Bi_2MoO_6 core–shell S-scheme heterojunction nanofibers for boosting visible-light catalytic levofloxacin degradation and Cr (VI) reduction," *Chemical Engineering Journal*, vol. 428, article 131158, 2022.

[33] X. Liu, G. Shaonan, Y. Zhao, G. Zhou, and W. Li, "$BiVO_4$, Bi_2WO_6 and Bi_2MoO_6 photocatalysis: a brief review," *Journal of Materials Science & Technology*, vol. 56, pp. 45–68, 2020.

[34] Z. Jun-Yu, L. Hong-Gang, and S. Shi-Gang, "Construction of 1D/1DWO_3nanorod/TiO_2 nanobelt hybrid heterostructure for photocatalytic application," *Chinese Journal of Structural Chemistry*, vol. 39, no. 6, pp. 1019–1028, 2020.

[35] J. Wang, G. Wang, B. Cheng, J. Yu, and J. Fan, "Sulfur-doped g-C_3N_4/TiO_2 S-scheme heterojunction photocatalyst for Congo Red photodegradation," *Chinese Journal of Catalysis*, vol. 42, no. 1, pp. 56–68, 2021.

[36] C. H. E. N. Yi-Lan, X. U. Yu-Xian, L. I. N. Dai-Feng, L. U. O. Yong-Jin, X. U. E. Hun, and C. H. E. N. Qing-Hua, "Insight into superior visible light photocatalytic activity for degradation of dye over corner-truncated cubic Ag_2O decorated TiO_2 hollow nanofibers," *Chinese Journal of Structural Chemistry*, vol. 39, no. 3, pp. 588–597, 2020.

[37] J. Zhao, S. Ge, D. Pan et al., "Solvothermal synthesis, characterization and photocatalytic property of zirconium dioxide doped titanium dioxide spinous hollow microspheres with sunflower pollen as bio-templates," *Journal of Colloid and Interface Science*, vol. 529, pp. 111–121, 2018.

[38] V. Ruíz-Santoyo, V. F. Marañon-Ruiz, R. Romero-Toledo, O. A. González Vargas, and A. Pérez-Larios, "Photocatalytic degradation of rhodamine B and methylene orange using TiO_2-ZrO_2 as nanocomposite," *Catalysts*, vol. 11, article 1035, 2021.

[39] K. Gurushantha, K. S. Anantharaju, S. C. Sharma et al., "Biomediated Sm doped nano cubic zirconia: photoluminescent, Judde Ofelt analysis, electrochemical impedance spectroscopy and photocatalytic performance," *Journal of Alloys and Compounds*, vol. 685, pp. 761–773, 2016.

[40] M. Ikram, R. Asghar, M. Imran et al., "Experimental and computational study of Zr and CNC-doped MnO_2 nanorods for photocatalytic and antibacterial activity," *ACS Omega*, vol. 7, no. 16, pp. 14045–14056, 2022.

[41] A. Ul-Hamid, M. Ikram, A. Haider et al., "In-situ phenylhydrazine chemical detection based on facile Zr-doped MoS_2 nanocomposites (NCs) for environmental safety," *Journal of the Taiwan Institute of Chemical Engineers*, vol. 120, pp. 267–277, 2021.

[42] M. Ikram, J. Hassan, A. Raza et al., "Photocatalytic and bactericidal properties and molecular docking analysis of TiO_2nanoparticles conjugated with Zr for environmental remediation," *RSC Advances*, vol. 10, no. 50, pp. 30007–30024, 2020.

[43] M. Ikram, R. Tabassum, U. Qumar et al., "Promising performance of chemically exfoliated Zr-doped MoS_2 nanosheets for catalytic and antibacterial applications," *RSC Advances*, vol. 10, no. 35, pp. 20559–20571, 2020.

[44] J. Kim, D. Rhee, O. Song et al., "All-solution-processed van der Waals heterostructures for wafer-scale electronics," *Advanced Materials*, vol. 34, no. 12, 2022.

[45] E. Kharatzadeh, S. R. Masharian, and R. Yousefi, "The effects of S-doping concentration on the photocatalytic performance of SnSe/S-GO nanocomposites," vol. 32, no. 2, pp. 346–357, 2021.

[46] M. R. Anil Kumar, B. Abebe, H. P. Nagaswarupa, H. C. Ananda Murthy, C. R. Ravikumar, and F. K. Sabir, "Enhanced photocatalytic and electrochemical performance of TiO_2-Fe_2O_3 nanocomposite: its applications in dye decolorization and as supercapacitors," *Scientific Reports*, vol. 10, no. 1, pp. 1–15, 2020.

[47] N. Montoya, P. Pardo, A. Doménech-Carbó, and J. Alarcón, "Structural stability and electrochemical properties of Gd-doped ZrO_2 nanoparticles prepared by sol–gel," *Journal of Sol-Gel Science and Technology*, vol. 69, no. 1, pp. 137–147, 2014.

[48] C. V. Reddy, I. N. Reddy, J. Shim, D. Kim, and K. Yoo, "Synthesis and structural, optical, photocatalytic, and electrochemical properties of undoped and yttrium-doped tetragonal ZrO_2 nanoparticles," *Ceramics International*, vol. 44, no. 11, pp. 12329–12339, 2018.

[49] K. Y. Zhang and Y. Zhai, "Preparation of Y-doped ZrO_2 coatings on MnO_2 electrodes and their effect on electrochemical performance for MnO_2 electrochemical supercapacitors," *RSC Advances*, vol. 6, pp. 1750–1759, 2016.

[50] N. Smirnova, Y. Gnatyuk, A. Eremenko et al., "Photoelectrochemical characterization and photocatalytic properties of mesoporous TiO_2/ZrO_2 films," *International Journal of Photoenergy*, vol. 2006, Article ID 85469, 6 pages, 2006.